

Raman Signatures of Broken Inversion Symmetry and In-Plane Anisotropy in Type-II Weyl Semimetal Candidate TaIrTe_4

Yinan Liu, Qiangqiang Gu, Yu Peng, Shaomian Qi, Na Zhang, Yinong Zhang, Xiumei Ma, Rui Zhu, Lianming Tong, Ji Feng,* Zheng Liu,* and Jian-Hao Chen*

The layered ternary compound TaIrTe_4 is an important candidate to host the recently predicted type-II Weyl fermions. However, a direct and definitive proof of the absence of inversion symmetry in this material, a prerequisite for the existence of Weyl Fermions, has so far remained evasive. Herein, an unambiguous identification of the broken inversion symmetry in TaIrTe_4 is established using angle-resolved polarized Raman spectroscopy. Combining with high-resolution transmission electron microscopy, an efficient and nondestructive recipe to determine the exact crystallographic orientation of TaIrTe_4 crystals is demonstrated. Such technique could be extended to the fast identification and characterization of other type-II Weyl fermions candidates. A surprisingly strong in-plane electrical anisotropy in TaIrTe_4 thin flakes is also revealed, up to 200% at 10 K, which is the strongest known electrical anisotropy for materials with comparable carrier density, notably in such good metals as copper and silver.

While considerable progress in both theory and experiment has been made on type-I Weyl semimetals,^[1,2,8] only a few type-II Weyl semimetals have been identified.^[5,9,10] TaIrTe_4 has recently been proposed to be a type-II Weyl semimetal candidate.^[7] As a ternary variant of WTe_2 , TaIrTe_4 is a layered material with interestingly strengthened Te–Te bonds and various possible crystal symmetry,^[11] referred to as the monoclinic ($1T'$ phase) and orthorhombic structures (T_d phase). While the monoclinic $1T'$ phase has the centrosymmetric space group $P2_1/m$, the orthorhombic T_d phase has two possible space groups, the non-centrosymmetric $Pmn2_1$ and the centrosymmetric $Pnmm$.^[12] The $Pmn2_1T_d$ phase TaIrTe_4 is predicted to host just four type-

The recent discovery of Weyl semimetals has attracted substantial attention among materials scientists and condensed matter physicists.^[1–3] It was predicted that two types of Weyl fermions^[4,5] may exist in solids with broken spatial inversion symmetry or time-reversal symmetry.^[2,6] In type-I Weyl semimetal, the bulk Fermi surface shrinks to a point at the Weyl node with conserved Lorentz invariance,^[7] whereas in type-II Weyl semimetal the Weyl points appear at the topologically protected touching points between electron and hole pockets with tilted Weyl cones.^[5]

II Weyl points, the minimal number of Weyl points hosted by a system with time-reversal invariance.^[7,10] Intensive efforts have been made to search for the related effects of the broken inversion symmetry and the type-II Weyl nodes of the material.^[2,6] However, the definitive signature of the broken spatial inversion symmetry or time-reversal symmetry in TaIrTe_4 has yet to be firmly established.^[13] Previous X-ray diffraction study was confronted with the uncertainty associated with subtle differences between the $Pmn2_1$ and the $Pnmm$ space groups.^[11] Recent pump-probe

Y. Liu, Q. Gu, S. Qi, Y. Zhang, Prof. J. Feng, Prof. J.-H. Chen
International Center for Quantum Materials
School of Physics
Peking University
No. 5 Yiheyuan Road, Beijing 100871, China
E-mail: jfeng11@pku.edu.cn; chenjianhao@pku.edu.cn

Dr. Y. Peng, Prof. Z. Liu
Centre for Programmed Materials
School of Materials Science and Engineering
Nanyang Technological University
Singapore 639798, Singapore
E-mail: z.liu@ntu.edu.sg


N. Zhang, Prof. L. Tong
College of Chemistry and Molecular Engineering
Peking University
No. 5 Yiheyuan Road, Beijing 100871, China

Dr. X. Ma, Dr. R. Zhu
Electron Microscopy Laboratory
School of Physics
Peking University
Beijing 100871, China

Prof. J. Feng
CAS Center for Excellence in Topological Quantum Computation
University of Chinese Academy of Sciences
Beijing 100190, China

Prof. J. Feng, Prof. J.-H. Chen
Collaborative Innovation Center of Quantum Matter
Beijing 100871, China

Prof. Z. Liu
NOVITAS
Nanoelectronics Centre of Excellence
School of Electrical and Electronic Engineering
Nanyang Technological University
Singapore 639798, Singapore

 The ORCID identification number(s) for the author(s) of this article can be found under <https://doi.org/10.1002/adma.201706402>.

DOI: 10.1002/adma.201706402

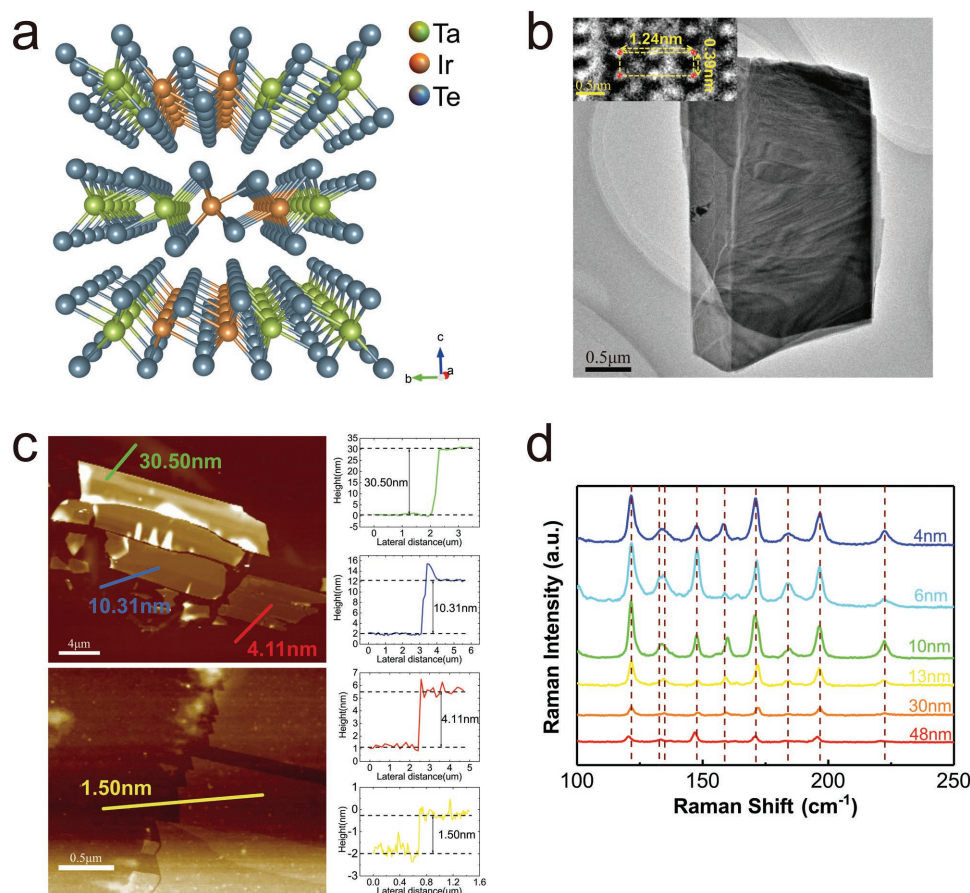


Figure 1. a) Crystal structure of TaIrTe₄. b) TEM image of a TaIrTe₄ thin flake. Inset: the corresponding HRTEM image of the TaIrTe₄ thin flake. c) AFM images of TaIrTe₄ flakes with various thickness. d) Unpolarized Raman spectra measured at TaIrTe₄ flakes of different thicknesses.

angle-resolved photoemission spectroscopy studies^[13,14] have observed hints of Weyl points and topological Fermi arcs in TaIrTe₄ with limited resolution, since the Weyl points and topological Fermi arcs are predicted to reside entirely above the Fermi level in TaIrTe₄.^[13] For transport studies, a negative longitudinal magnetoresistance, which signifies the chiral anomaly of Weyl Fermions, has not yet been observed in TaIrTe₄.^[15]

In this report, we use angle-resolved polarized Raman spectroscopy, which are directly sensitive to the crystal symmetry, to confirm unambiguously the absence of inversion symmetry in TaIrTe₄ bulk crystals as well as in its thin flakes. We observe strong optical and electrical in-plane anisotropy of few-layer TaIrTe₄ and provide a rapid and nondestructive method to identify the crystallographic orientation of TaIrTe₄. The in-plane electrical anisotropy of TaIrTe₄ thin flakes is found to be the strongest among materials with comparably high carrier density, which may enable new architectures in electrical interconnects in future integrated circuits. The results will prove valuable not only for further research into the physics and application of TaIrTe₄ but also for exploration of the family of type-II Weyl semimetals.

Figure 1a represents the side view of the TaIrTe₄ lattice structure. Alternating Ta–Ir connections stretch along the crystalline *a*-axis as zigzag atomic chains. These chains hybridize with each other along the *b*-direction to form a conducting *ab*-plane. A transmission electron microscopy (TEM) image of a TaIrTe₄

flake is shown in Figure 1b. Inset of Figure 1b is an atomically resolved TEM image of ultrathin TaIrTe₄, which shows clear orthogonal lattice fringes. The lattice constants of TaIrTe₄ can therefore be derived from this image: *a* = 0.39 nm and *b* = 1.24 nm, consistent with the results in the literature.^[11]

Few-layer TaIrTe₄ flakes were exfoliated mechanically and transferred onto a silicon substrate with 300 nm SiO₂. The flake thickness measured by atomic force microscopy (AFM) is shown in Figure 1c. Having a theoretical layer-to-layer spacing of 1.32 nm,^[11] we can clearly identify TaIrTe₄ with thicknesses down to around 1.5 nm in our AFM micrograph, corresponding to single unit cell of TaIrTe₄. In this work, we focus on flakes with ten layers or more with large enough size to perform optical and electrical measurements.

Figure 1d shows the thickness-dependent Raman spectra of TaIrTe₄ flakes. It can be seen that the Raman intensity of thin flakes (<20 nm) is relatively strong compared to the thick flakes (>20 nm). We attribute this phenomenon to the interference enhancement effect.^[16] Contrary to other layered materials, the position of the Raman peaks of TaIrTe₄ samples at different thicknesses did not change significantly.^[17] Throughout the rest of this study, we shall focus on the flakes with thickness less than 20 nm.

Figure 2a shows polarized Raman spectra (solid black curve) collected in a parallel polarization configuration from a 19 nm sample, where both the incident and scattered light polarize

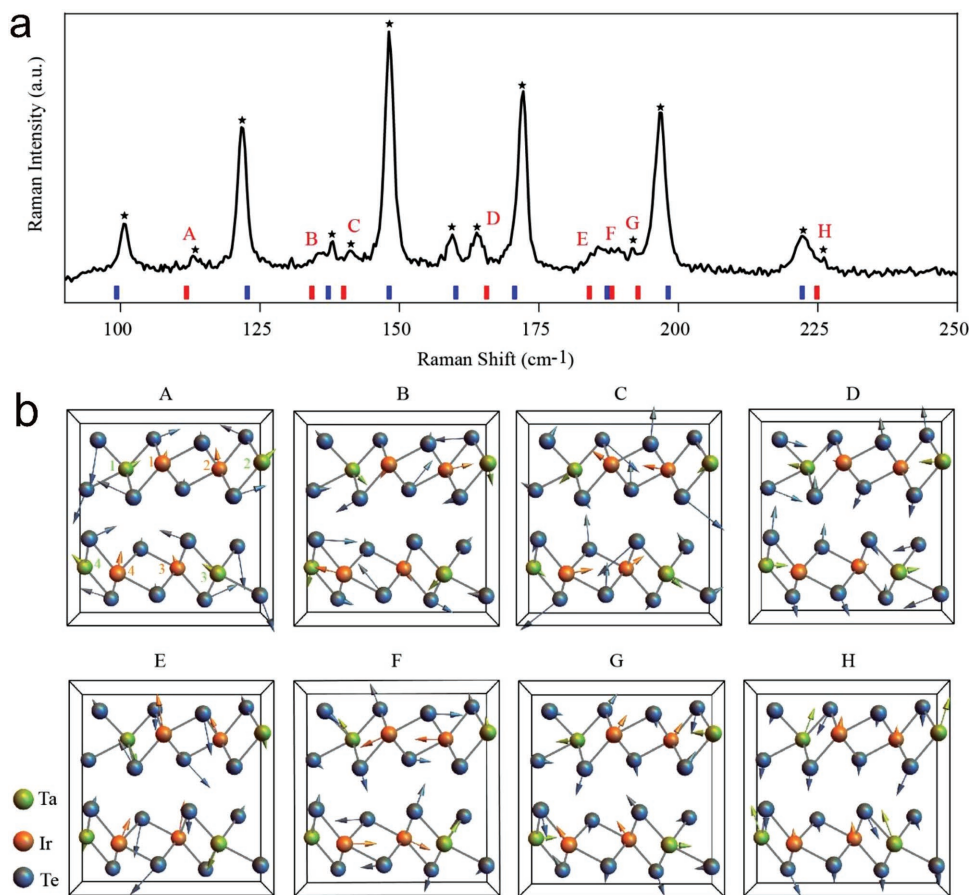


Figure 2. Polarized Raman spectra and phonon vibrational patterns. a) Polarized Raman spectra (solid black curve) with the parallel polarization configuration along *a*-axis and the respective calculated frequencies (vertical bars) of the A_1 representation phonons. The black stars show the central frequencies of the measured Raman peaks. b) Calculated phonon vibrational patterns for the Raman modes that are highlighted with red bars in (a). The green numbers 1–4 in vibrational pattern A denote the four Ta atoms and the orange number 1–4 denote the four Ir atoms in the unit cell, in which 1 and 2 denote the inversion equivalent atoms in the hypothetical inversion symmetric structure.

along the crystallographic *a*-axis. We shall focus on symmetry analysis here and discuss optical anisotropy as well as crystallographic directions of TaIrTe₄ in the next section.

Among the possible structures of TaIrTe₄, the only non-centrosymmetric structure belongs to the space group $Pmn2_1$ (point group C_{2v}). Thus, we first analyze the irreducible representations of group C_{2v} and make comparison with experimental data. The unit cell of TaIrTe₄ consists of 24 atoms, which support 72 phonon modes. Given the point group symmetry of the crystal, 69 optical phonons are Raman-active, which include $23A_1+12A_2+11B_1+23B_2$, where $A_{1,2}$ and $B_{1,2}$ are the irreducible representations of the point group C_{2v} .

For the given experimental configuration used to collect data in Figure 2a, only A_1 phonons are Raman active. The frequencies of all the A_1 phonon were determined by first-principles calculations and were indicated by red and blue vertical bars under the experimental Raman spectra in Figure 2a. It is evident that the frequencies of the experimental Raman peaks agree well with the calculations, with an uncertainty less than 0.46 meV in phonon energy.

In order to establish a direct connection between specific Raman signal and the broken inversion symmetry in the crystal, we invoke an analysis assuming the existence of

inversion center located in the TaIrTe₄ atomic layer between two Ir atoms (see Section S1, Supporting Information, for details). In this case, the point group of the crystal would become D_{2h} and the A_1 irreducible representation in point group C_{2v} splits into the parity-even A_g and the parity-odd B_{1u} representations in D_{2h} . The B_{1u} phonons are Raman inactive and thus should not be detected by Raman measurements. However, within the experimentally explored energy window, we have identified eight experimental Raman peaks that would belong to the B_{1u} irreducible representation in D_{2h} . These eight phonons are highlighted with red vertical bars in Figure 2a labeled by capital letters A–H, and their vibrational patterns are shown in Figure 2b. Note that some of these phonons (especially mode D) have strong Raman signals, indicating a strong inversion symmetry breaking, consistent with previously proposed, large Weyl node separation in TaIrTe₄.^[7] Mode D also has angle-dependence that matches perfectly with Raman tensor analysis (see Section S4, Supporting Information), excluding the possibility of defect signals. Thus, the observation of mode D in our polarized Raman experiments can be seen as a tell-tale signature of broken inversion symmetry, which makes TaIrTe₄ possible to be a type-II Weyl semimetal.

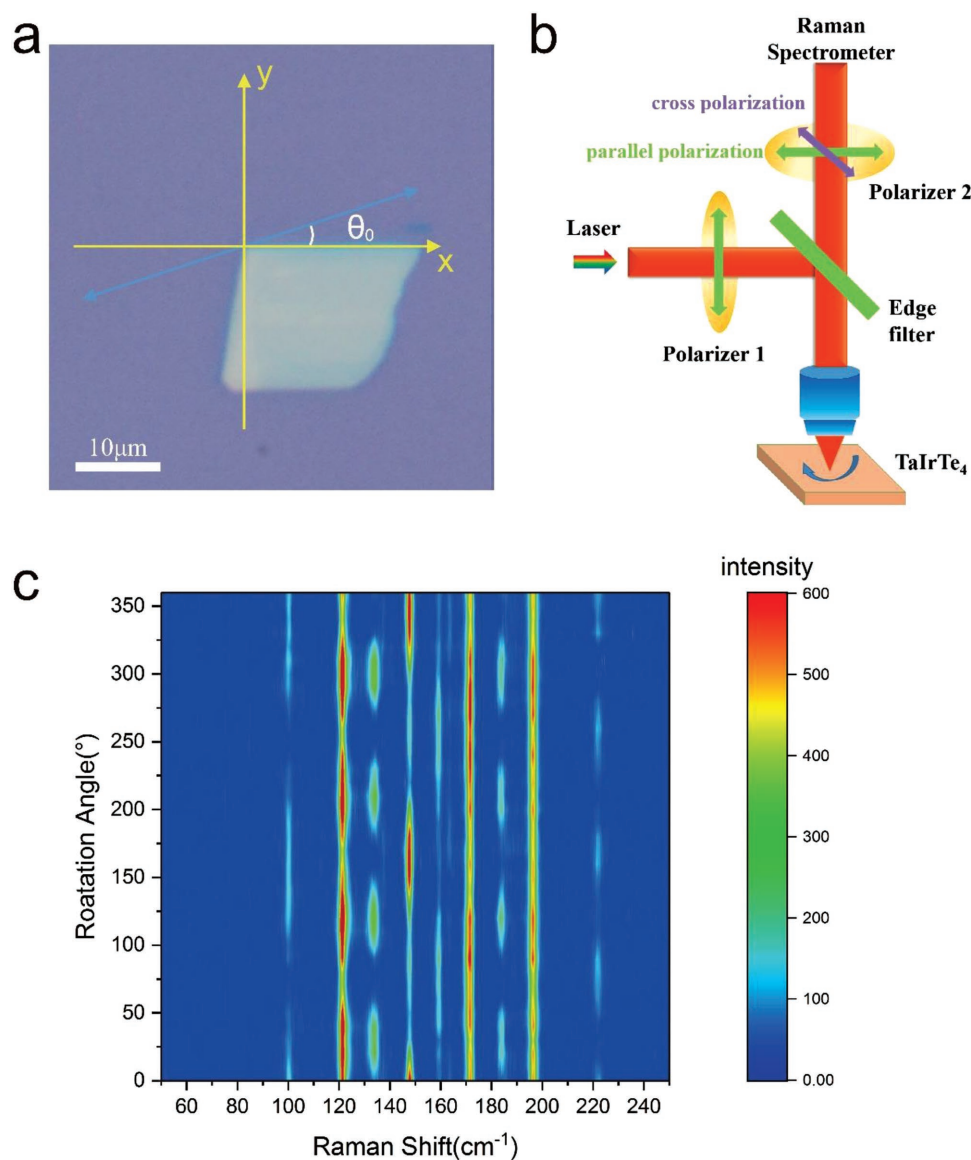


Figure 3. a) An optical image of a TaIrTe₄ flake with a thickness of around 12 nm. The blue double-headed arrow indicates the polarization of the incident light. b) Schematic diagram of the angle-resolved polarized Raman spectroscopy of TaIrTe₄ samples. c) Angular dependence of the intensity of the Raman spectra for a freshly exfoliated flake measured in parallel-polarized configuration.

Now we consider angle-resolved Raman spectra of the TaIrTe₄ samples. Freshly exfoliated thin TaIrTe₄ samples on 300 nm SiO₂ were mounted onto a rotation stage. The Raman spectra were taken using a 633 nm He-Ne laser. **Figure 3a** shows an optical image of a TaIrTe₄ flake with a thickness around 12 nm. The x -axis was assigned to be along the naturally occurring crystallographic edge as shown in **Figure 3a**. Later we will show that this edge indeed corresponds to the a -axis (zigzag direction of the Ta–Ir chains) of the TaIrTe₄ crystal. **Figure 3b** illustrates the experimental setup for the parallel-polarized and cross-polarized Raman scattering of the TaIrTe₄ samples. **Figure 3c** plots the angular dependences of the Raman intensity spectra in the parallel-polarized configuration. The results of the cross-polarized configuration are reported in **Figure S3** (Supporting Information). The sample rotation angle θ is in the range of 0° – 360° .

Figure 4 plotted in polar figures the intensity of six major Raman peaks evolving with angles in parallel-polarized configuration. Also shown are the atomic schematics of the corresponding phonon modes. Two types of modes are found in the parallel-polarized configuration. The first type has a two-lobed shape with two maximum intensities at angles $\theta = 180^\circ - \theta_0$ and $\theta = 360^\circ - \theta_0$ (θ_0 was used to denote the initial angle between the incident laser polarization and the x -axis); the second type has a four-lobed shape with maximum intensities at four angles. In the cross-polarized configuration, all modes yield four-lobed shapes (**Figure S3**, Supporting Information). Similar Raman spectra from TaIrTe₄ of two additional thicknesses are shown in **Figure S4** (Supporting Information). The results show that the anisotropic Raman spectra of TaIrTe₄ flakes have no clear thickness dependence for flakes thicker than 12 nm.

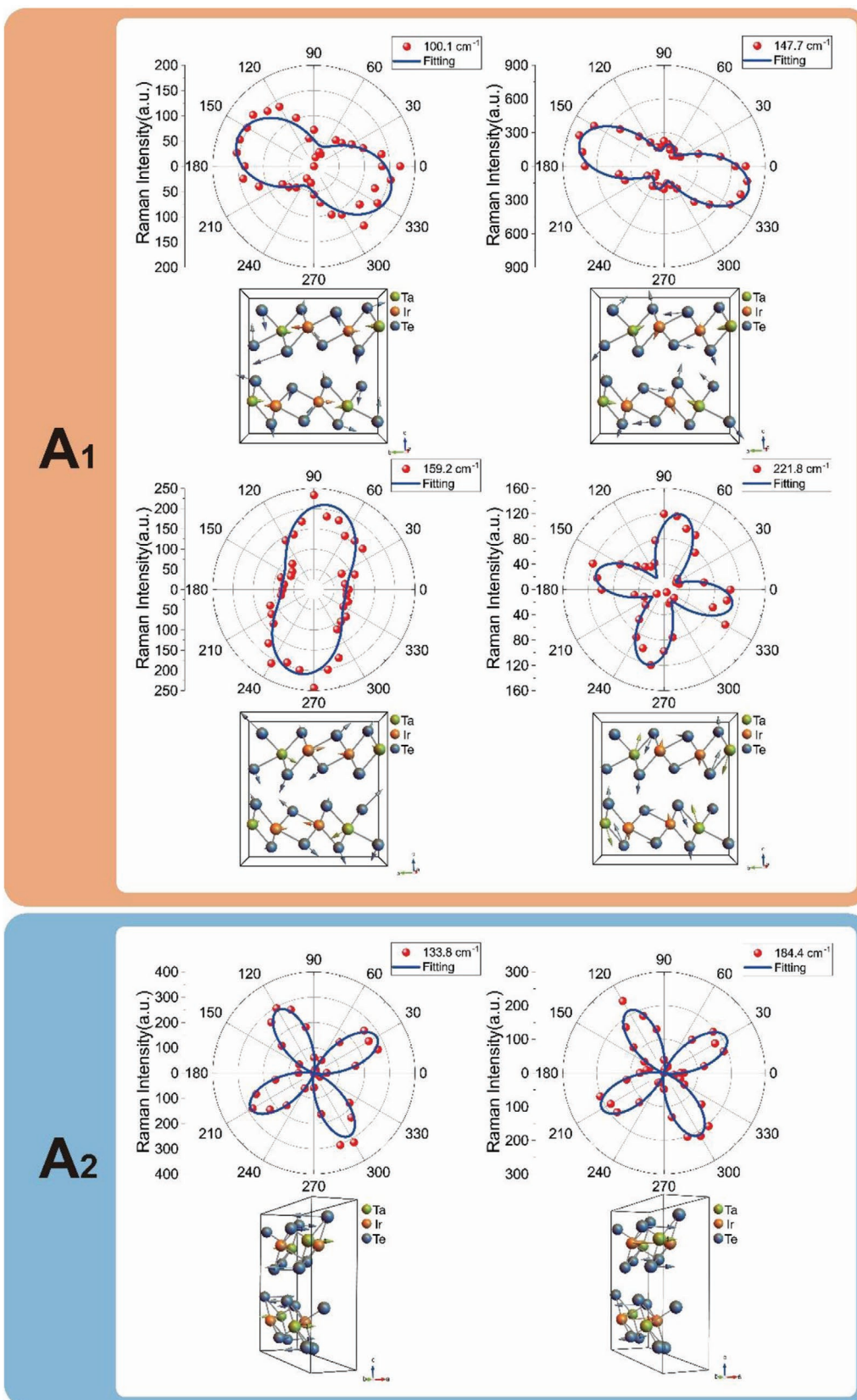


Figure 4. Raman intensities of six modes as a function of the sample rotation angle and the corresponding phonon modes in atomic view. The scattered dots are experimental data, and the solid lines are fitting curves.

Quantitative analysis on the observed anisotropic phenomena can be made, based on the group theory, from Raman tensors and density functional theory (DFT) calculations. The intensity of Raman signals from these modes can be expressed as^[18]

$$I \propto |\mathbf{e}_i \cdot \mathbf{R} \cdot \mathbf{e}_s|^2 \quad (1)$$

where \mathbf{e}_i and \mathbf{e}_s are the unit vectors of the incident and scattered light's polarization and \mathbf{R} is the Raman tensor for a certain vibration mode. The Raman tensors corresponding to the A_1 , A_2 , B_1 , and B_2 modes are^[19]

$$R_{A_1} = \begin{pmatrix} d & 0 & 0 \\ 0 & f & 0 \\ 0 & 0 & g \end{pmatrix} \quad R_{A_2} = \begin{pmatrix} 0 & h & 0 \\ h & 0 & 0 \\ 0 & 0 & 0 \end{pmatrix} \quad R_{B_1} = \begin{pmatrix} 0 & 0 & 0 \\ 0 & 0 & k \\ 0 & k & 0 \end{pmatrix} \quad (2)$$

$$R_{B_2} = \begin{pmatrix} 0 & 0 & l \\ 0 & 0 & 0 \\ l & 0 & 0 \end{pmatrix}$$

where $d, f, g, h, k,$ and l are the tensor elements determined by the cross section of Raman scattering.

In our experiment, the laser shines perpendicular to the (001) surface and thus for a sample with rotation angle θ , $\mathbf{e}_i = (\cos(\theta + \theta_0), \sin(\theta + \theta_0), 0)$ for the incident light, and $\mathbf{e}_s = (\cos(\theta + \theta_0), \sin(\theta + \theta_0), 0)$ for the scattered light in the parallel-polarized configuration.^[20] According to the backscattering geometry, only A_1 and A_2 modes have nonzero intensity.^[20] The angle-dependent intensity for the A_1 and A_2 modes can be expressed as

$$I_{A_1}^{\parallel} \propto d^2 \cos^4(\theta + \theta_0) + f^2 \sin^4(\theta + \theta_0) + 2df \cos^2(\theta + \theta_0) \sin^2(\theta + \theta_0) \cos 2\delta \quad (3)$$

$$I_{A_2}^{\parallel} \propto h^2 \sin^2 2(\theta + \theta_0) \quad (4)$$

Here, δ is a phase factor which accounts for the light absorption effect on the Raman tensor elements^[20,21] or the birefringence effect.^[22] We selected six relatively strong Raman peaks in parallel- and cross-polarized configurations, respectively, to fit to Equations (3) and (4). The fitted curves are in good agreement with the experimental data (Figure 4). In particular, possible effects from defects can be excluded from the angular dependence of the major Raman peaks as well as the stability of these peaks under ambient conditions^[23] (more discussions in Section S8, Supporting Information).

We find that the angular-dependent intensity for A_1 modes varied in periods of 180° and 90° in parallel-polarized configuration, while those for A_2 phonon modes varied in a period of 90° . In particular, the A_1 modes having a period of 180° could be used to determine the crystallographic orientation of the TaIrTe₄ lattice, since their intensity maxima are exactly along the a - or b -axis of the crystals. Whether the intensity maxima pointing to the a - or b -axis of the crystals depends on the relative magnitude of matrix elements in R_{A_i} for the specific phonon modes. Here, we use the Raman mode at 100 and 148 cm⁻¹ in parallel-polarized configurations to identify the zigzag direction of the crystal (i.e., the direction of Ta–Ir chains). For these two modes, if $d > f$, then the intensity maxima is along the a -axis; if $d < f$, then the intensity maxima is along the b -axis (see Section S5, Supporting Information, for

detailed analysis). We experimentally determined that $d > f$ in TaIrTe₄ by performing polarized Raman spectroscopy and high-resolution TEM (HRTEM) on the same flake. With this information, only polarized Raman spectroscopy is needed to rapidly and nondestructively identify the crystal orientation of TaIrTe₄ in future experiments. The recipe could be easily extended to other type-II Weyl semimetal candidates with in-plane anisotropy.^[20,24]

According to DFT calculations, the density of states of TaIrTe₄ at the Fermi level is very high.^[7] Experimentally, we measured a Hall density of $\approx 1.2 \times 10^{27} \text{ m}^{-3}$. In view of the large carrier density, one can consider TaIrTe₄ to be one of the good metals, which usually have isotropic conductivity.^[25] To our surprise, thin TaIrTe₄ samples exhibit extraordinarily strong electrical anisotropy, which is hitherto unprecedented among such good metals as copper and silver.

In order to study the electrical anisotropy of TaIrTe₄, we fabricated 12 electrodes (5 nm Cr/50 nm Au) on the same flake spaced at an angle of 30° along the directions as shown in Figure 5a and 0° is aligned roughly with the a -axis according to quantitative analysis based on the polarized Raman spectra. DC conductance was measured between each pair of diagonal contacts at different temperatures and the results are plotted in Figure 5b in polar coordinates. For an anisotropic material, the directional dependence of the low field conductivity can be described by the equation^[26]

$$\sigma_\theta = \sigma_x \cos^2(\theta - \phi) + \sigma_y \sin^2(\theta - \phi) \quad (5)$$

σ_x and σ_y refer to the conductivity along the (100) and (010) directions, respectively. θ is the angle of the applied current with respect to the 0° reference direction, along which both the electric field is applied and the conductance is measured; ϕ is the angle between the x -direction and the 0° reference. Equation (5) fits very well to the measured data (solid curves in Figure 5b). From the fitting, we obtained a ratio of σ_x/σ_y to be from 1.7 to 2.0 for temperature ranging from 300 to 10 K (Figure 5c). It is found that the a - and b -axes of the TaIrTe₄ thin film could be independently determined using the angle-resolved DC conductance measurement, with the maximum conductivity along the a -axis. In fact, the difference between the crystal orientations determined from the conductance measurement and from the polarized Raman spectroscopy is less than 5.6%. Another TaIrTe₄ device was measured at 300 K and presented similar anisotropic behavior (more details in Figure S6, Supporting Information).

To further understand the transport properties, we performed temperature-dependent Hall measurement along the a - and b -axes using the same device shown in Figure 5a. We attempted to obtain the ratio of Hall mobility (μ) and carrier concentrations (n) along the two directions. Since Hall resistivity can be expressed as $R_{xy} = -\frac{B}{ne}$, we can obtain the carrier concentrations from the slopes of the R_{xy} versus B curves taken at different directions. To extract the slope along the a -direction, a constant current I flows between leads 1 and 7 and the voltage V is measured between leads 4 and 10 when sweeping the magnetic field. Similarly, the slope of R_{xy} versus B along the b direction was obtained. We then use the formula $\sigma = ne\mu$ to get the ratio of the Hall mobilities. Figure 5c shows the temperature-dependent carrier concentration along a - and b -axes (n_a and n_b) and the inset shows n_a/n_b and μ_a/μ_b versus temperature.

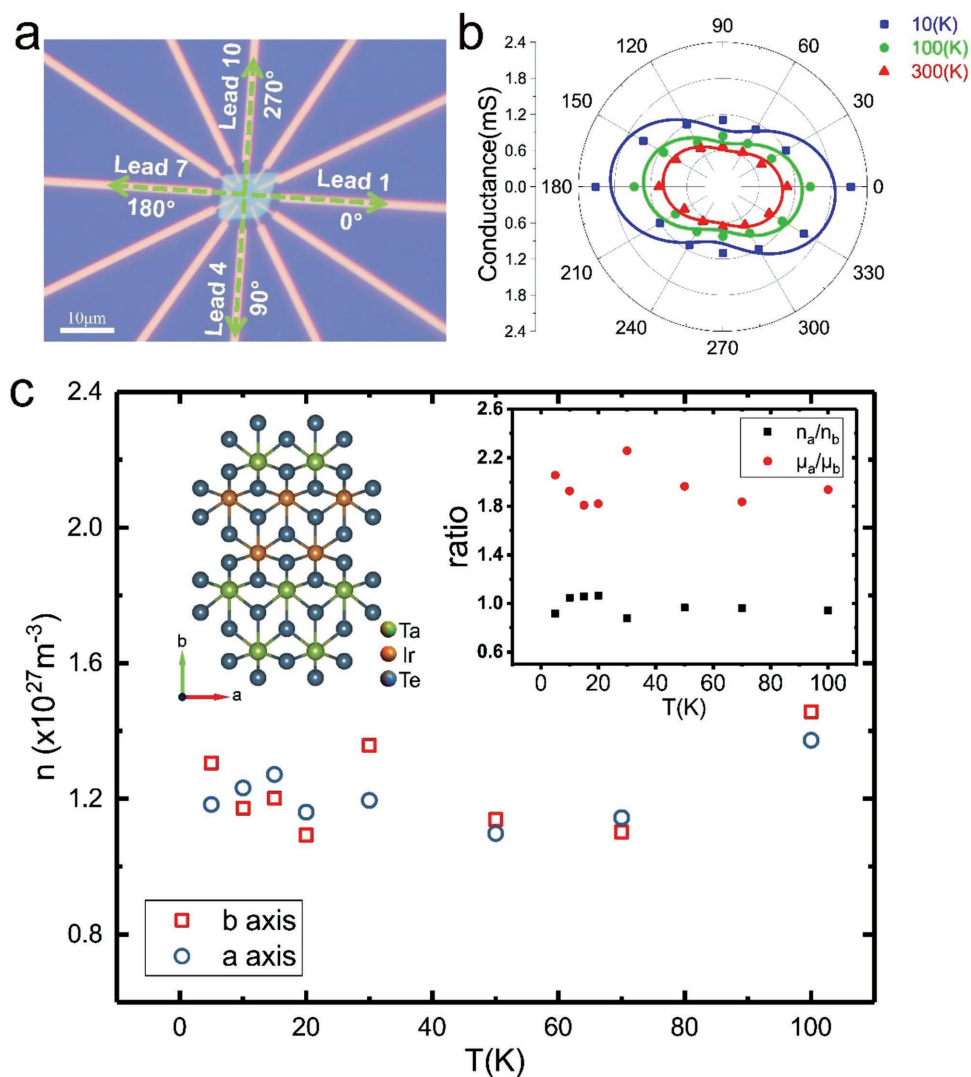


Figure 5. Angle-resolved DC conductance measurements of TaIrTe₄ thin flakes. a) An optical image of the TaIrTe₄ thin flake device. b) Angle-dependent DC conductance at different temperatures. c) Temperature-dependent carrier concentration measured along *a*- and *b*-axes. Upper left inset: atomic top view of the *ab*-plane of the TaIrTe₄ crystal; upper right inset: the ratio of Hall mobilities along *a*- and *b*-axes at different temperatures.

While the carrier concentrations remain the same along the two directions, a significant difference arises from the Hall mobility. Since the anisotropy in mobility decreases as temperature increases, we can exclude phonon scattering as the origin of the electrical anisotropy. A likely explanation of the anisotropy is the different effective masses along the two principle axes of the TaIrTe₄ crystals.^[27] Such strong electrical anisotropy, together with the high carrier density and the environmental stability of the material (see Section S5, Supporting Information for stability study of TaIrTe₄ thin flakes), may enable new architectures in electrical interconnects in future integrated circuits.^[28]

In summary, we provide the first definitive evidence for the absence of inversion symmetry of the TaIrTe₄ crystals, by combining linearly polarized Raman spectroscopy and first-principle calculations. Our result shows that TaIrTe₄ could indeed be a type-II Weyl semimetal. We also demonstrate an efficient and nondestructive recipe to determine the exact crystallographic orientation

of TaIrTe₄ crystals and other anisotropic type-II Weyl semimetal candidates. The in-plane electrical anisotropy of TaIrTe₄ thin flakes is found to be the strongest among materials with comparably high carrier density, which may enable new architectures in electrical interconnects in future integrated circuits.

Experimental Section

The Growth of TaIrTe₄ Single Crystal: All the used elements were stored and acquired in argon-filled glove box with moisture and oxygen levels less than 0.1 ppm, and all manipulations were carried out in the glove box. TaIrTe₄ single crystals were synthesized by solid-state reaction with the help of Te flux. The elements of Ta powder (99.99%), Ir powder (99.999%), and Te lump (99.999%) with an atomic ratio of Ta/Ir/Te = 1:1:12, purchased from Sigma-Aldrich (Singapore), were loaded in a quartz tube and then flame-sealed under high vacuum of 10⁻⁶ torr. The quartz tube was placed in a tube furnace, slowly heated up to 1000 °C and held for 100 h, and then allowed to cool to 600 °C at a rate of 0.8 °C h⁻¹, followed by a cool down to room temperature.

The shiny, needle-shaped TaIrTe₄ single crystals can be obtained from the product.

Raman Spectroscopy: The polarized Raman spectra were obtained on an HR 800 (Jobin Yvon Horiba), with a 632.8 nm laser. A polarizer was used to select the incident polarization and was fixed during all the measurements. Another adjustable polarizer was added before the spectrometer to form the parallel-polarized and the cross-polarized configurations. Raman measurements were carried out in ambient conditions, since the TaIrTe₄ flakes are fairly air stable (more details in Figure S7, Supporting Information).^[29]

First-Principles Calculations: The ab initio calculations were carried out using the Vienna ab initio simulation package (VASP)^[30] with the local density approximation (LDA)^[31] and the projector augmented wave (PAW) potentials.^[32] The kinetic energy cutoff is fixed to 400 eV, and the *k*-point mesh is taken as 8 × 2 × 2. The coordinates and the cell shape were fully relaxed until the forces acting on the atoms are all smaller than 10⁻⁴ eV Å⁻¹. The small displacement method implemented in phonopy package^[33] was used to get the phonon frequencies and vibration modes at the Γ point.

Device Fabrication and Characterization: Standard electron-beam lithography technique was used to pattern electrodes, consisting of 5 nm Cr and 50 nm Au, on the TaIrTe₄ samples to form devices. Electrical anisotropy measurements were carried out in a homemade low-temperature ultrahigh vacuum system with standard lock-in technique.

Supporting Information

Supporting Information is available from the Wiley Online Library or from the author.

Acknowledgements

Y.N.L. and Q.Q.G. contributed equally to this work. This project was supported by the National Basic Research Program of China (973 Grant Nos. 2013CB921900, 2014CB920900, and 2016YFA0301004), and the National Natural Science Foundation of China (NSFC Grant Nos. 11374021, 11774010, 11725415, and 21573004) (Y.N.L., Q.Q.G., S.M.Q., N.Z., Y.N.Z., L.M.T., Y.P., J.F., and J.-H.C.). Y.P. and Z.L. acknowledge support from Singapore National Research Foundation (NRF RF Award No. NRF-RF2013-08) and MOE Tier 2 grant MOE2016-T2-1-131 (S). J.F. acknowledges support from the Key Research Program of the Chinese Academy of Sciences (Grant No. XPD08-4). Y.N.L. and J.-H.C. conceived the experiment. Y.N.L. exfoliated the TaIrTe₄ thin flakes, fabricated the devices, completed AFM, Raman, and transport measurements, and analyzed the data. N.Z. helped with the Raman measurements under the supervision of L.M.T. X.M.M. and R.Z. performed TEM measurements. Q.Q.G. and J.F. performed the first-principle calculations. Y.P. and Z.L. provided high-quality bulk TaIrTe₄ crystals. Y.N.L., Q.Q.G., S.M.Q., Y.N.Z., J.F., Z.L., and J.-H.C. discussed the results and analyzed the data. Y.N.L., Q.Q.G., S.M.Q., J.F., Z.L., and J.-H.C. wrote the manuscript and all authors commented on it.

Conflict of Interest

The authors declare no conflict of interest.

Keywords

2D material, DFT calculations, in-plane anisotropy, Raman spectroscopy, type-II Weyl semimetal

Received: November 3, 2017
Revised: February 10, 2018
Published online: May 7, 2018

- [1] A. A. Burkov, L. Balents, *Phys. Rev. Lett.* **2011**, *107*, 127205.
- [2] X. G. Wan, A. M. Turner, A. Vishwanath, S. Y. Savrasov, *Phys. Rev. B* **2011**, *83*, 205101.
- [3] a) M. N. Ali, J. Xiong, S. Flynn, J. Tao, Q. D. Gibson, L. M. Schoop, T. Liang, N. Haldolaarachchige, M. Hirschberger, N. P. Ong, R. J. Cava, *Nature* **2014**, *514*, 205; b) X. Huang, L. Zhao, Y. Long, P. Wang, D. Chen, Z. Yang, H. Liang, M. Xue, H. Weng, Z. Fang, X. Dai, G. Chen, *Phys. Rev. X* **2015**, *5*, 031023; c) B. Q. Lv, H. M. Weng, B. B. Fu, X. P. Wang, H. Miao, J. Ma, P. Richard, X. C. Huang, L. X. Zhao, G. F. Chen, Z. Fang, X. Dai, T. Qian, H. Ding, *Phys. Rev. X* **2015**, *5*, 031013; d) H. Weng, C. Fang, Z. Fang, B. A. Bernevig, X. Dai, *Phys. Rev. X* **2015**, *5*, 011029; e) S. Y. Xu, I. Belopolski, N. Alidoust, M. Neupane, G. Bian, C. L. Zhang, R. Sankar, G. Q. Chang, Z. J. Yuan, C. C. Lee, S. M. Huang, H. Zheng, J. Ma, D. S. Sanchez, B. K. Wang, A. Bansil, F. C. Chou, P. P. Shibayev, H. Lin, S. Jia, M. Z. Hasan, *Science* **2015**, *349*, 613; f) S. M. Huang, S. Y. Xu, I. Belopolski, C. C. Lee, G. Q. Chang, B. K. Wang, N. Alidoust, G. Bian, M. Neupane, C. L. Zhang, S. Jia, A. Bansil, H. Lin, M. Z. Hasan, *Nat. Commun.* **2015**, *6*, 7373.
- [4] H. Weyl, *Z. Phys.* **1929**, *56*, 330.
- [5] A. A. Soluyanov, D. Gresch, Z. J. Wang, Q. S. Wu, M. Troyer, X. Dai, B. A. Bernevig, *Nature* **2015**, *527*, 495.
- [6] a) S. Murakami, *New J. Phys.* **2007**, *9*, 356; b) P. Hosur, X. L. Qi, C. R. Phys. **2013**, *14*, 857; c) A. M. Turner, A. Vishwanath, arXiv:1301.0330, **2013**.
- [7] K. Koepnik, D. Kasinathan, D. V. Efremov, S. Khim, S. Borisenko, B. Buchner, J. van den Brink, *Phys. Rev. B* **2016**, *93*, 201101(R).
- [8] G. Xu, H. M. Weng, Z. J. Wang, X. Dai, Z. Fang, *Phys. Rev. Lett.* **2011**, *107*, 186806.
- [9] a) S. Y. Xu, N. Alidoust, G. Q. Chang, H. Lu, B. Singh, I. Belopolski, D. S. Sanchez, X. Zhang, G. Bian, H. Zheng, M. A. Husanu, Y. Bian, S. M. Huang, C. H. Hsu, T. R. Chang, H. T. Jeng, A. Bansil, T. Neupert, V. N. Strocov, H. Lin, S. A. Jia, M. Z. Hasan, *Sci. Adv.* **2017**, *3*; b) S. Borisenko, D. Evtushinsky, Q. Gibson, A. Yaresko, T. Kim, M. N. Ali, B. Buechner, M. Hoesch, R. J. Cava, *Physics* **2015**; c) Y. Sun, S. C. Wu, M. N. Ali, C. Felser, B. H. Yan, *Phys. Rev. B* **2015**, *92*, 161107(R); d) G. Q. Chang, S. Y. Xu, D. S. Sanchez, S. M. Huang, C. C. Lee, T. R. Chang, G. Bian, H. Zheng, I. Belopolski, N. Alidoust, H. T. Jeng, A. Bansil, H. Lin, M. Z. Hasan, *Science Adv.* **2016**, *2*, e1600295.
- [10] Z. J. Wang, D. Gresch, A. A. Soluyanov, W. W. Xie, S. Kushwaha, X. Dai, M. Troyer, R. J. Cava, B. A. Bernevig, *Phys. Rev. Lett.* **2016**, *117*, 056805.
- [11] A. Mar, S. Jobic, J. A. Ibers, *J. Am. Chem. Soc.* **1992**, *114*, 8963.
- [12] a) C. J. Bradley, A. P. Cracknell, *The Mathematical Theory of Symmetry in Solids*, Clarendon, Oxford **1972**; b) G. F. Koster, *Solid State Phys.: Adv. Res. Appl.* **1957**, *5*, 173.
- [13] I. Belopolski, M. Z. Hasan, P. Yu, arXiv:1610.02013, **2016**.
- [14] E. Haubold, K. Koepnik, D. Efremov, S. Khim, A. Fedorov, Y. Kushnirenko, J. van den Brink, S. Wurmehl, B. Buchner, T. K. Kim, M. Hoesch, K. Sumida, K. Taguchi, T. Yoshikawa, A. Kimura, T. Okuda, S. V. Borisenko, *Phys. Rev. B* **2017**, *95*, 241108(R).
- [15] a) I. Belopolski, D. S. Sanchez, Y. Ishida, X. C. Pan, P. Yu, S. Y. Xu, G. Q. Chang, T. R. Chang, H. Zheng, N. Alidoust, G. Bian, M. Neupane, S. M. Huang, C. C. Lee, Y. Song, H. J. Bu, G. H. Wang, S. S. Li, G. Eda, H. T. Jeng, T. Kondo, H. Lin, Z. Liu, F. Q. Song, S. Shin, M. Z. Hasan, *Nat. Commun.* **2016**, *7*; b) Y. J. Wang, E. F. Liu, H. M. Liu, Y. M. Pan, L. Q. Zhang, J. W. Zeng, Y. J. Fu, M. Wang, K. Xu, Z. Huang, Z. L. Wang, H. Z. Lu, D. Y. Xing, B. G. Wang, X. G. Wan, F. Miao, *Nat. Commun.* **2016**, *7*.
- [16] a) Y. Y. Wang, Z. H. Ni, Z. X. Shen, H. M. Wang, Y. H. Wu, *Appl. Phys. Lett.* **2008**, *92*, 043121; b) X. Ling, J. Zhang, *J. Phys. Chem. C* **2011**, *115*, 2835.

- [17] a) Z. B. Yang, W. J. Jie, C. H. Mak, S. H. Lin, H. H. Lin, X. F. Yang, F. Yan, S. P. Lau, J. H. Hao, *ACS Nano* **2017**, *11*, 4225; b) I. Stenger, L. Schue, M. Boukhicha, B. Berini, B. Placais, A. Loiseau, J. Barjon, *2D Mater.* **2017**, *4*.
- [18] R. Loudon, *Adv. Phys.* **1964**, *13*, 423.
- [19] a) W. D. Kong, S. F. Wu, P. Richard, C. S. Lian, J. T. Wang, C. L. Yang, Y. G. Shi, H. Ding, *Appl. Phys. Lett.* **2015**, *106*, 081906; b) Y. C. Jiang, J. Gao, L. Wang, *Sci. Rep.* **2016**, *6*.
- [20] Q. J. Song, X. C. Pan, H. F. Wang, K. Zhang, Q. H. Tan, P. Li, Y. Wan, Y. L. Wang, X. L. Xu, M. L. Lin, X. G. Wan, F. Q. Song, L. Dai, *Sci. Rep.* **2016**, *6*, 29254.
- [21] M. Kim, S. Han, J. H. Kim, J. U. Lee, Z. Lee, H. Cheong, *2D Mater.* **2016**, *3*, 034004.
- [22] a) N. N. Mao, J. X. Wu, B. W. Han, J. J. Lin, L. M. Tong, J. Zhang, *Small* **2016**, *12*, 2627; b) S. Zhang, N. Mao, N. Zhang, J. Wu, L. Tong, J. Zhang, *ACS Nano* **2017**, *11*, 10366.
- [23] S. Y. Chen, C. H. Naylor, T. Goldstein, A. T. C. Johnson, J. Yan, *ACS Nano* **2017**, *11*, 814.
- [24] a) F. N. Xia, H. Wang, Y. C. Jia, *Nat. Commun.* **2014**, *5*, 4458; b) R. He, J. A. Yan, Z. Y. Yin, Z. P. Ye, G. H. Ye, J. Cheng, J. Li, C. H. Lui, *Nano Lett.* **2016**, *16*, 1404; c) K. N. Zhang, C. H. Bao, Q. Q. Gu, X. Ren, H. X. Zhang, K. Deng, Y. Wu, Y. Li, J. Feng, S. Y. Zhou, *Nat. Commun.* **2016**, *7*; d) X. M. Wang, A. M. Jones, K. L. Seyler, V. Tran, Y. C. Jia, H. Zhao, H. Wang, L. Yang, X. D. Xu, F. N. Xia, *Nat. Nanotechnol.* **2015**, *10*, 517; e) S. Y. Chen, T. Goldstein, D. Venkataranan, A. Ramasubramaniam, J. Yan, *Nano Lett.* **2016**, *16*, 5852.
- [25] a) N. W. Ashcroft, N. D. Mermin, *Solid State Physics*, Harcourt College Publishers, Orlando **1976**; b) C. Kittel, *Introduction to Solid State Physics*, Wiley, New York **2005**.
- [26] a) G. Qiu, Y. C. Du, A. Charnas, H. Zhou, S. Y. Jin, Z. Luo, D. Y. Zemlyanov, X. F. Xu, G. J. Cheng, P. D. D. Ye, *Nano Lett.* **2016**, *16*, 7364; b) W. Yu, Y. Jiang, J. Yang, Z. L. Dun, H. D. Zhou, Z. Jiang, P. Lu, W. Pan, *Sci. Rep.* **2016**, *6*.
- [27] a) D. Chen, L. X. Zhao, J. B. He, H. Liang, S. Zhang, C. H. Li, L. Shan, S. C. Wang, Z. A. Ren, C. Ren, G. F. Chen, *Phys. Rev. B* **2016**, *94*, 174411; b) S. H. Khim, K. Koepernik, D. V. Efremov, J. Klotz, T. Forster, J. Wosnitza, M. I. Sturza, S. Wurmehl, C. Hess, J. van den Brink, B. Buchner, *Phys. Rev. B* **2016**, *94*, 165145; c) X. L. Xu, Q. J. Song, H. F. Wang, P. Li, K. Zhang, Y. L. Wang, K. Yuan, Z. C. Yang, Y. Ye, L. Dai, *ACS Appl. Mater. Interfaces* **2017**, *9*, 12601.
- [28] a) P. S. Bhardwaj, P. U. Sathyakam, P. Karthikeyan, A. Karthikeyan, *Imp. J. Interdiscip. Res.* **2016**, *2*; b) A. Hosseini, V. Shabro, *Microelectron. Eng.* **2010**, *87*, 1955.
- [29] H. M. Oh, G. H. Han, H. Kim, J. J. Bae, M. S. Jeong, Y. H. Lee, *ACS Nano* **2016**, *10*, 5230.
- [30] G. Kresse, J. Furthmuller, *Phys. Rev. B* **1996**, *54*, 11169.
- [31] J. P. Perdew, A. Zunger, *Phys. Rev. B* **1981**, *23*, 5048.
- [32] G. Kresse, D. Joubert, *Phys. Rev. B* **1999**, *59*, 1758.
- [33] A. Togo, I. Tanaka, *Scr. Mater.* **2015**, *108*, 1.